Influence of Pumping Beam Width on VECSEL Output Power

Adam K. Sokół and Robert P. Sarzała

Abstract—The paper is devoted to a numerical analysis of an influence of a pumping beam diameter on output power of optically pumped vertical-external-cavity surface-emitting lasers. Simulations have been carried out for a structure with a GaInNAs/GaAs active region operating at 1.32 µm. Various assembly configurations have been considered. Results obtained show that laser power scaling is strongly affected by thermal properties of the device.

Keywords—VECSEL, SDL, semiconductor disk laser, simulation, numerical modeling, power scaling

I. INTRODUCTION

OPTICALLY pumped vertical-external-cavity surface-emitting lasers (VECSELs) are semiconductor lasers which combine advantages of vertical-cavity surface-emitting lasers (high quality output beams), edge-emitting lasers (high output powers) and solid-state disk lasers (optical pumping) [1]. Moreover, an external cavity enables placing additional optical elements in a laser resonator including nonlinear crystals for frequency doubling or semiconductor saturable absorber mirrors (SESAMs) for ultrashort pulse generation. Because of their unique properties VECSELs can find broad applications, for example in medical, telecom and multimedia markets.

An important advantage of optical pumping is a possibility of increasing laser output power without changing its geometry, shape or principle of operation. This feature is commonly known as power scaling [2]–[4]. If we assume that the VECSEL semiconductor structure can be treated as a two-dimensional array of very small and independent "emitters" (cf. Fig. 1), it will turns out that overall emitted power is proportional to a cross-sectional area of the emitted laser beam. This means that laser output power can be increased by increasing a diameter of pumping and emitted beams and without changing the laser design. However, the real power scalability is strongly limited especially by thermal properties of the device [4], [5]. Heat flow within the laser volume is never ideally one-dimensional, which causes that the individual "emitters" are not fully independent of each other. Therefore laser output power is not generally proportional to the cross-sectional area of the emitted beam. In the paper an influence of the laser beam diameter on laser output power has been investigated with the aid of the self-consistent numerical model. Simulations have been carried out for the GaInNAs/GaAs VECSEL in different assembly configurations.

All the authors are with the Photonics Group, Institute of Physics, Lodz University of Technology, Wolczanska 219, 90-924 Łódź, Poland (e-mails: adam.sokol@p.lodz.pl, robert.sarzala@p.lodz.pl).
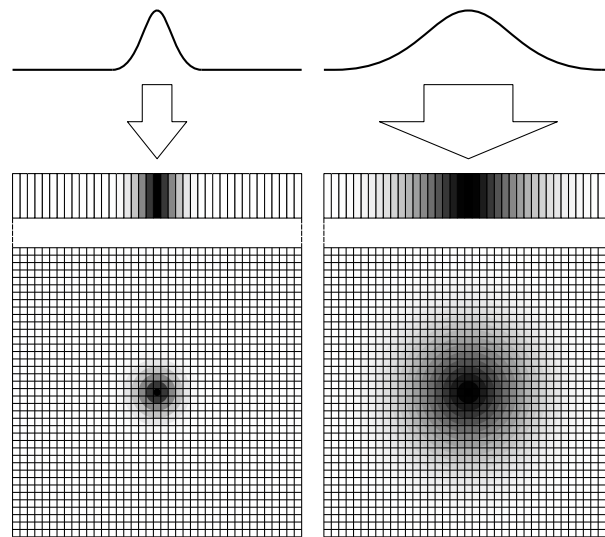
Fig. 1. The VECSEL semiconductor structure can be treated as the 2D array of very small and independent "emitters"

Results obtained show that thermal properties of the device have an important influence on laser power scalability.

II. LASER STRUCTURES

The simulated structure has been designed on the basis of the multi-quantum well GaInNAs/GaAs laser emitting at 1.32 µm and described in the paper [6]. It is placed on the GaAs substrate – its thickness has been assumed to be equal to 450 µm. The active region consists of five pairs of 7-nm $Ga_{0.63}In_{0.37}N_{0.012}As_{0.988}$ quantum wells (QWs) separated in each pair by a 13-nm one and between pairs by 158-nm GaAs barriers to form the resonant-periodic-gain (RPG) structure. Over the active region, there are the upper 282-nm window $Al_{0.3}Ga_{0.7}As$ layer and the 10-nm cap GaAs layer. The DBR mirror is composed of 25.5 periods of the quarter-wave GaAs/AlAs layers. The laser structure is mounted on the water-cooled copper heat sink with the aid of the 125-µm thick indium foil. Three different assembly configurations have been considered: BHS – without the substrate and with the Bottom Heat Spreader, UHS – with the substrate and the Upper Heat Spreader, DHS – with the Double Heat Spreader. All configurations are schematically shown in Fig. 2. The heat spreaders are made of the 270-µm (upper) and 300-µm (bottom) natural diamond plates. The upper heat spreader is bonded to the laser surface using the capillary action of distilled water, while the bottom one is attached to the semiconductor structure with the aid of thin 5-µm thick indium solder. Structures with
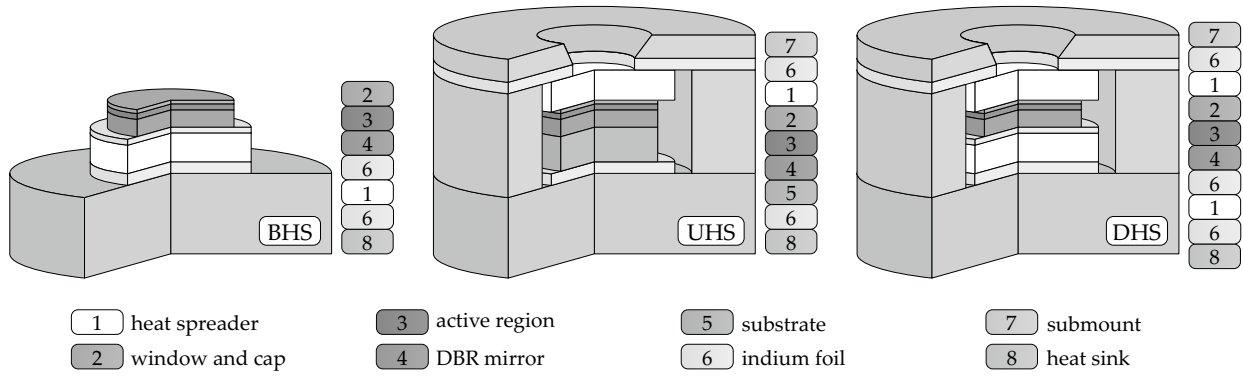
Fig. 2. Assembly configurations of the modeled structure. BHS – bottom heat spreader, UHS – upper heat spreader, DHS – double heat spreader
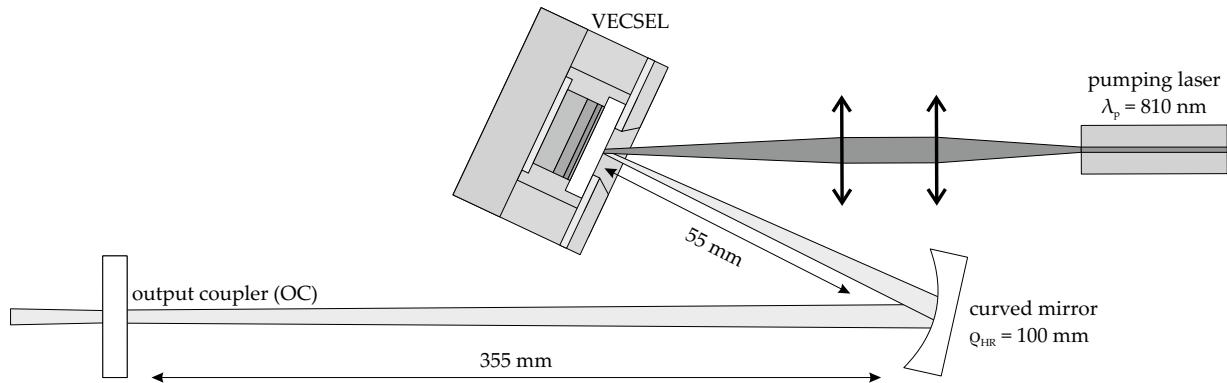

Fig. 3. External V-shape cavity

the upper heat spreaders are additionally closed in copper submounts providing proper mechanical stability as well as better extraction of heat generated in the active region. All considered structures are pumped by the fiber-coupled diode array emitting at 810 nm. The Gaussian intensity profile of the pumping beam is assumed. The complete laser structure is placed in the V-shape cavity with a curved mirror positioned 55 mm from the sample and an output coupler (OC) positioned 355 mm from the curved mirror (Fig. 3). Transmission of the output coupler is 2% and the temperature of the bottom heat sink surface is assumed to be $5\,^\circ$C for the UHS and DHS structures and $-10\,^\circ$C for the BHS one (due to high thermal resistance of the laser in BHS configuration, lasing threshold was not achieved at $5\,^\circ$C).

III. NUMERICAL MODEL

All calculations have been carried out with the aid of the self-consistent model developed in the Photonics Group, Institute of Physics, Lodz University of Technology. The model consists of four strongly interrelated modules for calculations of: heat flow, material gain, carrier transport and optical phenomena. All these modules are fully compatible and can be used as separate blocks as well as the one self-consistent complex model. The simplified block diagram of this model is presented in Fig. 4. The unquestionable advantage of the self-consistent approach is a possibility of an accurate analysis of complex interrelations between individual physical processes

taking place within laser structures, which is often difficult to examine using experimental methods. Individual model parts have been shortly described below.

A. Thermal Module

Knowledge of a temperature distribution within the laser structure is very important in VECSEL simulations as the majority of parameters used in carrier transport, gain and optical model parts are temperature-dependent. Such a distribution may be obtained by solving the 3D Fourier-Kirchhoff heat transfer equation in the cylindrical (r, z) coordinate system [7]:

$$\nabla \cdot [k(r, z)\nabla(T(r, z))] = -G(r, z) \qquad (1)$$

where $k(r, z)$ is the thermal conductivity coefficient, T is temperature and $G(r, z)$ is the volumetric power density of heat generation. The finite-element method (FEM) is used to solve the above equation. Assuming proper boundary conditions we can consider convective as well as radiative heat transfer between the modeled structure and its surroundings. The strong advantage of our model is a possibility of determination of the exact temperature distribution not only in a semiconductor chip but also in other laser parts such as: heat sinks, heat spreaders, submounts, solders, assembly foils and so on. Moreover, the thermal dependence of thermal conductivity coefficients for individual laser layers is taken into account. Therefore calculations have to be carried out in the self-consistent regime.

www.czasopisma.pan.pl

PAN
POLSKA AKADEMIA NAUK

www.journals.pan.pl

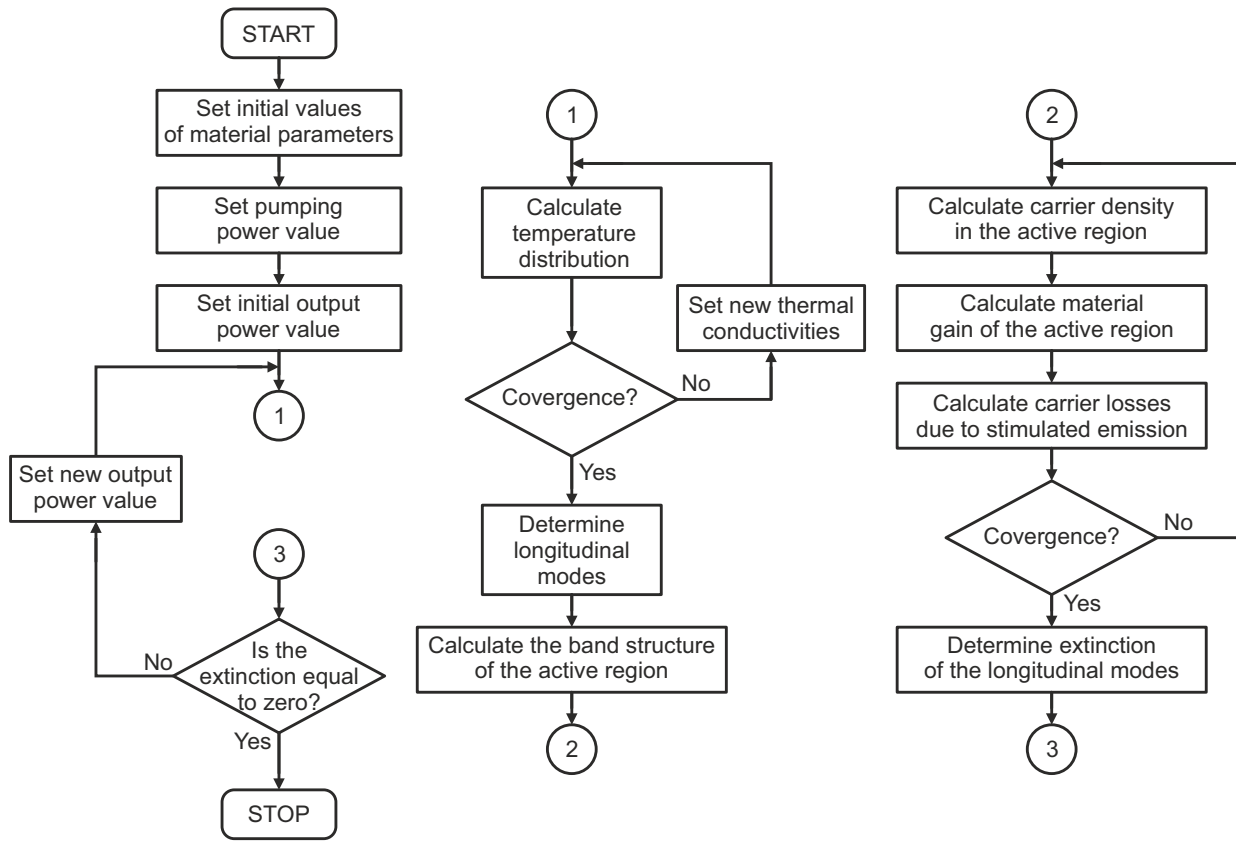INFLUENCE OF PUMPING BEAM WIDTH ON VECSEL OUTPUT POWER

241

Fig. 4. Simplified block diagram of the VECSEL simulation model developed by the Photonics Group, Institute of Physics, Lodz University of Technology

B. Gain Module

Material gain of quantum wells is calculated utilizing Fermi Golden Rule [8] in parabolic-band approximation. The following equation can be written:

$$g\left(\hbar\omega\right) = \sum_m \int_{-\infty}^{\infty} g_m\left(\epsilon\right) \Lambda\left(\hbar\omega - \epsilon\right) d\epsilon \qquad (2)$$

where i denotes number of available level pairs and:

$$g_m\left(\hbar\omega\right) = \frac{e^2 \pi \rho_r^{2D}\left(\hbar\omega\right)|M|^2}{n_R \epsilon_0 m_0^2 c\omega} \cdot$$
$$\cdot \left\{f_c\left[E_e\left(m,\hbar\omega\right)\right] - f_v\left[E_e\left(m,\hbar\omega\right)\right]\right\} \quad (3)$$

In above relations, e is the electron charge, $\hbar$ – the Dirac constant, ω – photon angular frequency, m_0 – electron rest mass, n_R – refractive index of the QW material, ϵ_0 – is the vacuum permittivity, M – the momentum matrix element, ρ_r^{2D} – two-dimensional reduced density of states, f_c and f_v stand for the Fermi-Dirac functions determined for electrons in the conduction band and holes in the valence band, respectively, E_e and E_h are the energies of the recombining electron and hole, respectively, and Λ is the broadening function, usually of Lorentzian type. The band structure of the active region is calculated with the aid of the model presented in [9]. Strains both in QWs and barriers are taken into account.

C. Optical module

The optical module bases on the Transfer Matrix Method (TMM), which enables quick calculations of reflectivity and longitudinal modes for simple one-dimensional structures. Assuming that the laser layers are normal to the z axis and the electric field within the jth layer can be represented as the superposition of down- and up-traveling waves with a wave number k:

$$E\left(z\right) = E_j^+ \exp\left(ik_j z\right) + E_j^- \exp\left(-ik_j z\right) \qquad (4)$$

where E_j^+ and E_j^- are amplitudes of traveling waves. Propagation through the jth layer to the $(j+1)$th one is described by the transfer matrix T_j:

$$\begin{bmatrix} E_{j+1}^+ \\ E_{j+1}^- \end{bmatrix} = T_j \begin{bmatrix} E_j^+ \\ E_j^- \end{bmatrix} \qquad (5)$$

where

$$2T_j = \begin{bmatrix} \exp\left(-id_j k_j\right)\left(1 + \frac{k_j}{k_{j+1}}\right) & \exp\left(id_j k_j\right)\left(1 - \frac{k_j}{k_{j+1}}\right) \\ \exp\left(-id_j k_j\right)\left(1 - \frac{k_j}{k_{j+1}}\right) & \exp\left(id_j k_j\right)\left(1 + \frac{k_j}{k_{j+1}}\right) \end{bmatrix} \qquad (6)$$

where d_j is the jth layer thickness. Propagation through the multi-layer structure with N layers is described by the following transfer matrix:

$$T = \begin{bmatrix} T_{00} & T_{01} \\ T_{10} & T_{11} \end{bmatrix} = T_{N-1} \cdot T_{N-2} \cdot \ldots \cdot T_1 \cdot T_0 \qquad (7)$$

Assuming appropriate boundary conditions in the first and last layers we can determine reflectivity as well as longitudinal modes for the considered structure.

242

www.czasopisma.pan.pl

PAN
POLSKA AKADEMIA NAUK

www.journals.pan.pl

A. K. SOKÓŁ, R. P. SARZAŁA

D. Carrier Transport Module

A typical structure of an optically pumped VECSEL contains an active region with several QWs separated by relatively long barrier layers. The exponential character of an absorption of pumping radiation results in non-homogeneous excitation of the QWs. Therefore it is necessary to consider the carrier transport in the vertical direction along the whole active region to determine the carrier density in each QW. Our model assumes that the QWs are reduced to points and act as carrier absorbers [10]. To calculate the carrier density distribution along the active region with N QWs separated by $N-1$ internal barriers and surrounded by two external ones, the following one-dimensional diffusion equation with no carrier drift contribution has to be solved for each barrier [11]:

$$D\frac{d^2 n_b}{dz^2} - n_b\left(A + Bn_b + Cn_b^2\right) + \frac{q_a\alpha_p\lambda_p}{hc}\exp\left(-\alpha_p z\right) = 0 \tag{8}$$

where D is the ambipolar diffusion coefficient, n_b stands for the carrier density in the barrier, z is the vertical coordinate, A, B, C are monomolecular, bimolecular and Auger recombination coefficients, respectively, λ_p is the pumping wavelength, α_p – the absorption coefficient for pumping radiation, h – the Planck constant, c – the speed of light in vacuum, q_a – the surface power density of pumping radiation entering the active region. Solutions of Eq. (8) for individual barriers are connected assuming that there is no carrier flow outside of the active region and the carrier density is continuous at each QW. Carrier losses in the jth QW can be calculated using the steady-state carrier balance equation:

$$J_L^{(j)} - J_R^{(j)} = d_{QW}^{(j)}\left(An_{QW}^{(j)} + Bn_{QW}^{(j)2} + Cn_{QW}^{(j)3} + L_{st}^{(j)}\right) \tag{9}$$

where $J_L^{(j)}$ and $J_R^{(j)}$ represent the carrier flux density into the continuous states above the QW from the left and right side, respectively. Symbol d_{QW} stands for the QW thickness and n_{QW} – for the carrier density in the QW, which may be determined by finding the quasi-Fermi levels and calculating the density integrals. $L_{st}^{(j)}$ in Eq. (9) is the component responsible for stimulated emission losses [12] in the jth QW:

$$L_{st}^{(j)} = \frac{q_e}{E_e \cdot d_{QW}^{(j)}} \cdot \frac{g_{QW}^{(j)} \cdot \Gamma^{(j)}}{g_c\Gamma_c} \tag{10}$$

where q_e is the surface power density of emitted radiation, E_e – the energy of the emitted photon, $d_{QW}^{(j)}$ – QW thickness, $g_{QW}^{(j)}$ – QW material gain, $\Gamma^{(j)}$ – QW confinement factor, g_c – total gain in the active region, Γ_c – total confinement factor for the active region. Index "th" indicates the threshold value of the $g_c\Gamma_c$ product. The $\Gamma^{(j)}$ for the jth QW is:

$$\Gamma^{(j)} = \frac{\left|E_{(j)}^+\exp\left(ik_{(j)}z_{QW}^{(j)}\right) + E_{(j)}^-\exp\left(-ik_{(j)}z_{QW}^{(j)}\right)\right|^2}{\left|E_0^+\right|^2 + \left|E_0^-\right|^2} \tag{11}$$

where $E_{(j)}^+$ and $E_{(j)}^-$ are the electric fields of down- and up-traveling waves in the jth QW and E_0^+ and E_0^- are the analogous electric fields in the surrounding medium (air in our case). The total confinement factor Γ_c is the sum of $\Gamma^{(j)}$ for all QWs in the active region.

TABLE I
MATERIAL PARAMETERS AT 300 K USED IN SIMULATIONS. FITTING PARAMETERS ARE DENOTED WITH ASTERISKS

Monomolecular recombination coefficient*	$3.6 \cdot 10^9$ 1/s
Bimolecular recombination coefficient	$3 \cdot 10^{-11}$ cm³/s [14]
Auger recombination coefficient	$6 \cdot 10^{-29}$ cm⁶/s [14]
Diffusion coefficient	10 cm²/s [15]
GaAs thermal conductivity	44.1 W/(mK) [16]
AlAs thermal conductivity	90.0 W/(mK) [17], [18]
AlGaAs thermal conductivity	12.2 W/(mK) [16], [18]
GaInNAs thermal conductivity	4.5 W/(mK) [19]
Indium thermal conductivity	81.3 W/(mK) [20]
Copper thermal conductivity	400.8 W/(mK) [21]
Diamond thermal conductivity	2200 W/(mK) [22], [23]
Diamond contact thermal conductivity*	0.77 W/(mK)
GaAs refractive index at 1300 nm	3.41 [24]
AlAs refractive index at 1300 nm	2.91 [25], [26]
AlGaAs refractive index at 1300 nm	3.24 [24]
GaInNAs refractive index at 1300 nm	3.8 [27]
Absorption coefficient at 810 nm	10000 1/cm [11]
Internal losses*	10 cm^{-1}
Scattering coefficient of the air-GaAs interface*	0.25%
Scattering coefficient of the air-diamond interface*	0.25%
Scattering coefficient of the diamond-GaAs interface*	0.35%

E. Parameters

Table I lists material parameters at 300 K used in simulations. Spectral and temperature dependences of the parameters can be found in references given in the table. The model has been calibrated using experimental results for the structure in the UHS configuration from [6]. The monomolecular recombination coefficient, internal losses and scattering coefficients of air-cap, air-heat spreader and heat spreader-cap interfaces have been used as fitting parameters. Moreover, to take into account the non-ideal thermal connection between the upper diamond heat spreader and the semiconductor structure, it has been assumed that there is a 10-nm thick contact layer between these two elements. Thermal conductivity of this layer has been numerically estimated to fit the experimental results from [6]. Parameters and relations for the gain calculations can be found in the reference [13].

IV. RESULTS

First, thermal properties of the modeled laser in different assembly configurations have been studied. Figure 5 shows relation between thermal resistance and pumping beam diameter. The ratio of pumping power to the pumping beam cross-sectional area (average pumping power density) is kept at constant value $2.26 \cdot 10^8$ Wm^{-2} in the whole considered range of pumping beam widths. Thermal resistance is defined as the ratio of maximal temperature increase to overall power of heat sources within the laser volume. The Gaussian intensity profile of the pumping beam and the $1/e^2$ definition of the beam

width have been assumed. Gray curves in Fig. 5 correspond to the theoretical ideally scalable structure for which laser output power is proportional to cross-sectional area of the pumping beam (assuming that diameters of pumping and emitted beams are equal). For such a structure the temperature increase at the constant pumping beam density is independent of the pumping beam width. One can see that for all considered assembly configurations thermal resistance of the device decreases when increasing the pumping beam diameter, however, this decrease is significantly lower as compared with the ideally scalable structure. For the UHS structure there is even an increase of thermal resistance for pumping beams of diameter higher than 900 μm. This behavior is connected with a decrease of thermal conductivity of the diamond heat spreader resulting from a temperature increase. For narrow pumping beams the BHS structure has the worst thermal properties among all considered configurations. However, for beams of diameter higher than 600 μm, the thermal resistance of this structure is lower as compared with the UHS structure. Such a behavior can be explained in the following way. For wider pumping beams, the heat flow from the laser active region to the heat sink is almost one-dimensional. Such a heat transport is naturally less efficient than the two-dimensional flow for narrow beams. This results in an increase in temperature while increasing the pumping beam width keeping the constant pumping power density. For narrow pumping beams, heat sources are strongly condensed near the laser axis, so it is very important to spread this heat in the lateral directions before it can be extracted by the heat sink. In this case, an application of the upper heat spreader located closely to the active region contributes to a significant improve of laser thermal properties. For wider pumping beams heat spreading is not such important as the one-dimensional heat flow towards the heat sink. In this case substrate removing and application of the bottom heat spreader give better results. Thermal resistance of the laser can be significantly reduced by applying both approaches, however this significantly increases the cost of the device. Nevertheless, none of the considered assembly configurations can provide an ideal scalability of the modeled laser.

This means that VECSEL power scaling is determined by two contrary mechanisms competing with each other. On the one hand, increasing pumping beam width causes that more "emitters" (cf. Fig. 1) are involved in laser action and generation of laser radiation. This should result in higher output power. On the other hand, the increase in pumping beam width (at the constant density of pumping power) leads to deterioration of laser thermal properties. High thermal resistance causes that the gain spectrum of the active region shifts faster towards the longer wavelengths. Moreover, high temperature increase results in the decrease of maximal available material gain of QWs (at the constant carrier density) and contributes to more intensive thermal escape of carriers from QWs. This impairs the laser performance. Therefore, one can reach a conclusion that there should be an optimal value of the pumping beam diameter which provides the most effective laser operation and highest output power.

Figure 6 shows power transfer characteristics – relations between power emitted through the output coupler $\left(P_{\mathrm{e}}^{\mathrm{OC}}\right)$ and
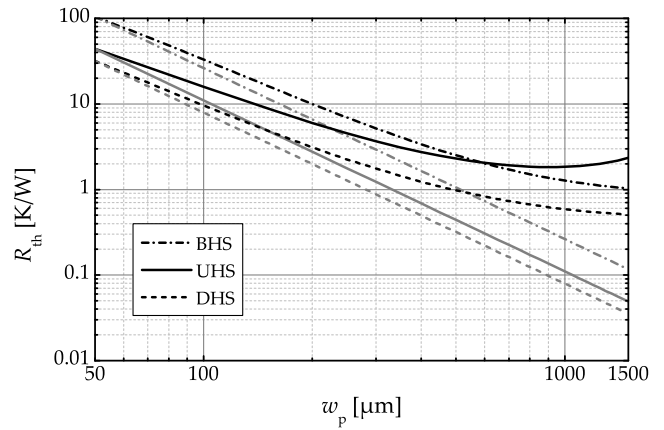

Fig. 5. Thermal resistance of the laser in various configurations (black curves) versus pumping beam width for the constant pumping power density $2.26 \cdot 10^{8}\ \mathrm{Wm}^{-2}$. Grey curves denote the ideally scalable structure
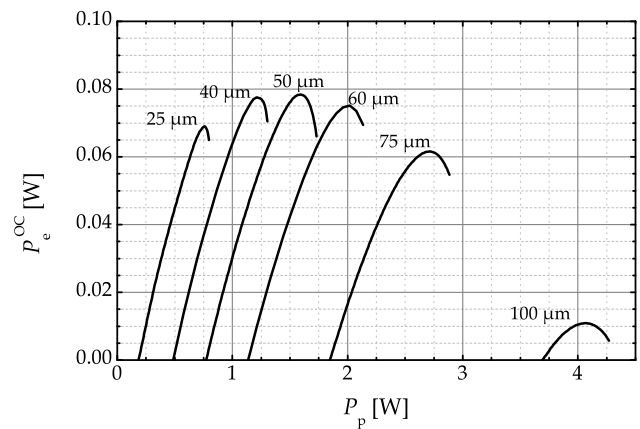

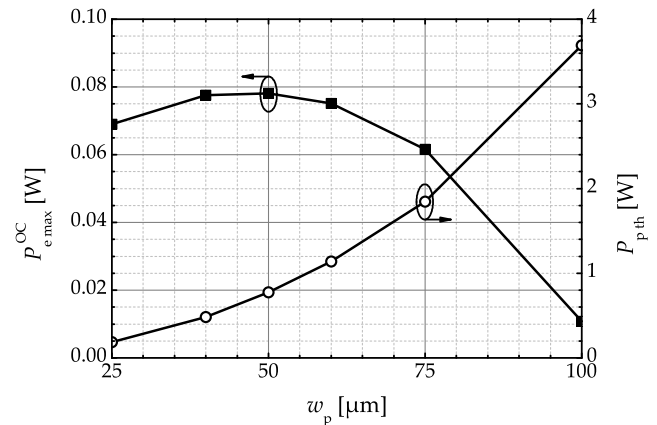Fig. 6. Power transfer characteristics of the BHS structure for different beam widths

Fig. 7. Maximal output power (left axis) and threshold power (right axis) versus beam width for the BHS structure

pumping power (P_{p}) – for the structure in the BHS configuration for different pumping beam widths. In calculations it has been assumed that the emitted beam has the same diameter as the pumping beam. In this case the highest output power has been achieved for the 50-μm pumping beam. This value determines the limit of the laser scalability. Increasing the

pumping beam diameter (e.g. to 75 or 100 μm) leads to the decrease in output power. This results from deterioration of laser thermal properties caused by less effective extraction of the heat flux from the active region. Together with the increase in the pumping beam width the threshold pumping power also increases, however, this increase is significantly higher than for the ideally scalable structure. For the ideally scalable structure increasing the beam diameter by two times should result in increasing threshold value of pumping power by four times. For the considered structure in the BHS configuration the increase in threshold power is significantly higher (e.g. changing the diameter of the pumping beam from 50 μm to 100 μm results in threshold power increased by factor of 4.8). This can be seen in Fig. 7 showing maximal output power $\left(P_{\mathrm{e}}^{\mathrm{OC}}\right)$ and threshold power $(P_{\mathrm{p\,th}})$ of the BHS structure as a function of the pumping beam diameter.

Application of the diamond plate on the laser upper surface results in a significant improve of the laser thermal properties for the narrow pumping beams. As it has been shown in Fig. 5, for beams of diameter lower than 600 μm thermal resistance of the UHS structure can be even two times lower then thermal resistance of the BHS structure. Higher efficiency of heat-flux extraction contributes to better power scalability. Figure 8 shows power transfer characteristics of the laser in the UHS configuration for different pumping beam widths. In this case the highest power has been achieved for the pumping beam of diameter of 125-μm. Further increase in pumping beam width leads to the decrease in laser output power. The main limitation of power scaling are, like in the case of the BHS configuration, thermal properties of the device. Power scaling for pumping beams of diameter lower than 125 μm is also not ideal. For the ideally scalable structure changing the beam diameter from 50 μm to 125 μm (by 2.5 times) enables obtaining 6.25-times higher output power. In the case of the considered UHS structure the analogous increase corresponds to factor lower than two. It can be seen in Fig. 9 presenting maximal output power and threshold pumping power of the UHS structure as a function of the pumping beam diameter. Similarly to the BHS structure, the increase in threshold power is higher than for the ideally scalable structure. However, it is clear, that the improvement in the thermal properties of the laser results in the significant increase in effectiveness of power scaling.

The best results have been obtained for the structure in the DHS configuration. Such an approach combines virtues of both previous configurations. The upper diamond increases the efficiency of spreading heat generated in the active region, whereas the lack of the substrate and application of the bottom heat spreader contribute to more effective transport of this heat to the copper heat sink. This means that the DHS structure has relatively low thermal resistance in the whole range of considered beam diameters. As it can be seen in Fig. 10, maximal output power has been achieved for the pumping beam of 270 μm diameter. Changing the pumping beam width from 75 μm to 270 μm results in increasing laser output power by a factor of 3.5. For the ideally scalable structure the analogous factor should be about 11. However, the application of double heat spreader still causes the significant improvement in laser
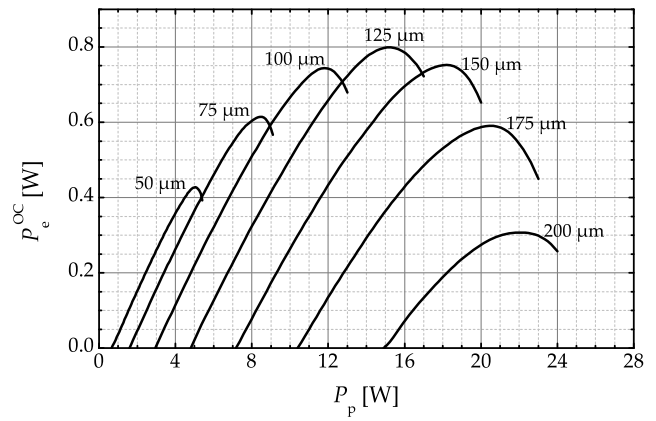

Fig. 8. Power transfer characteristics of the UHS structure for different beam widths
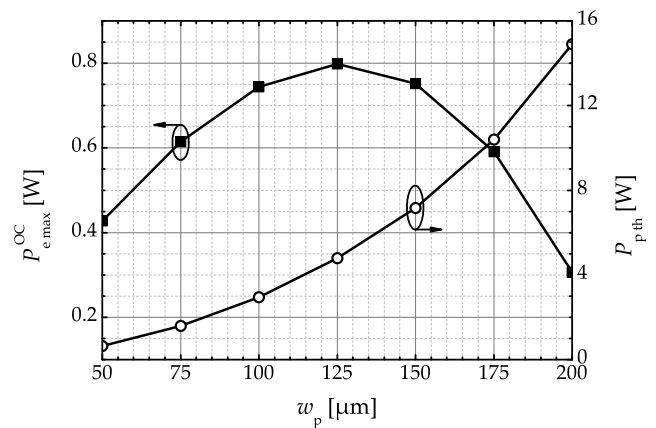

Fig. 9. Maximal output power (left axis) and threshold power (right axis) versus beam width for the UHS structure
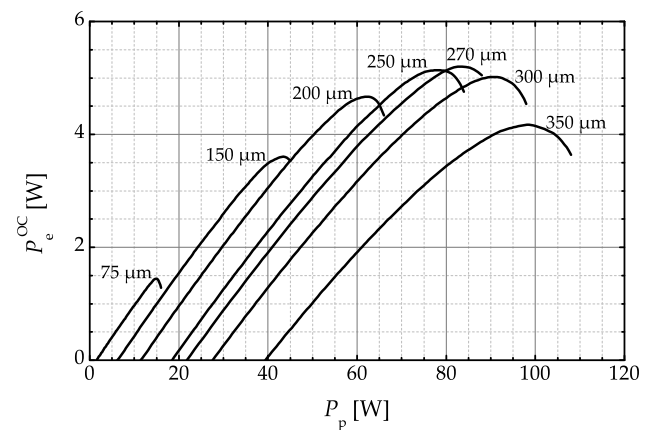

Fig. 10. Power transfer characteristics of the DHS structure for different beam widths

scalability in relation to the BHS and UHS configurations. Maximal output power and threshold pumping power of the DHS structure as a function of the beam diameter have been shown in Fig. 11.
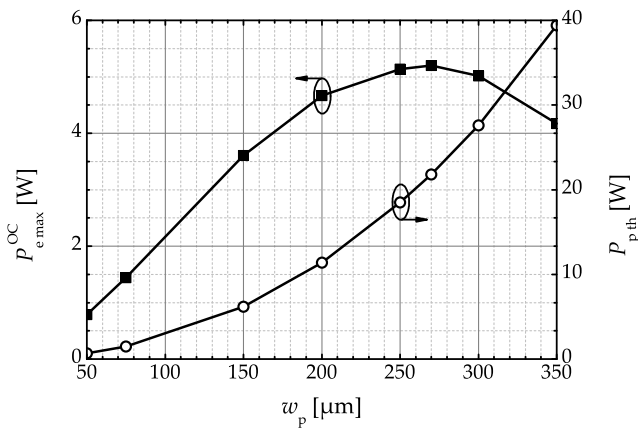
www.czasopisma.pan.pl

PAN

www.journals.pan.pl

POLSKA AKADEMIA NAUK

INFLUENCE OF PUMPING BEAM WIDTH ON VECSEL OUTPUT POWER

245

Fig. 11. Maximal output power (left axis) and threshold power (right axis) versus beam width for the DHS structure

V. CONCLUSION

Power scaling is an important advantage of optically pumped VECSELs. It gives a possibility of increasing laser output power without changing the geometry of the semiconductor structure. However, power scaling is strongly limited by thermal properties of the device. Increasing the pumping beam diameter results in decreasing efficiency of heat extraction. In the paper influence of pumping beam diameter on laser power transfer characteristics has been studied with the aid of self-consistent numerical model. Three various assembly configuration have been considered. The best performance has been achieved in the double diamond configuration, which provides the lowest thermal resistance of the modeled laser. In this case the maximal output power was 66.6 times higher than for the BHS structure at $-10\,°C$ and 6.5 higher than for the UHS structure at $5\,°C$.

REFERENCES

[1] O. G. Okhotnikov, Ed., *Semiconductor Disk Lasers: Physics and Technology*. Weinheim: Wiley-VCH, 2010.

[2] S. Chatterjee, A. Chernikov, J. Herrmann, M. Scheller, M. Koch, B. Kunert, W. Stolz, S. W. Koch, T.-L. Wang, Y. Kaneda, J. M. Yarborough, J. Hader, and J. V. Moloney, "Power scaling and heat management in high-power vecsels," in *Lasers and Electro-Optics Europe (CLEO EUROPE/EQEC), 2011 Conference on and 12th European Quantum Electronics Conference*, May 2011.

[3] S. Lutgen, T. Albrecht, P. Brick, W. Reill, J. Luft, and W. Spth, "8-W high-efficiency continuous-wave semiconductor disk laser at 1000 nm," *Applied Physics Letters*, vol. 82, no. 21, pp. 3620–3622, 2003.

[4] A. Chernikov, J. Herrmann, M. Scheller, M. Koch, B. Kunert, W. Stolz, S. Chatterjee, S. W. Koch, T.-L. Wang, Y. Kaneda, J. M. Yarborough, J. Hader, and J. V. Moloney, "Influence of the spatial pump distribution on the performance of high power vertical-external-cavity surface-emitting lasers," *Applied Physics Letters*, vol. 97, no. 19, pp. 191 110–191 110–3, Nov 2010.

[5] T.-L. Wang, Y. Kaneda, J. M. Yarborough, J. Hader, J. V. Moloney, A. Chernikov, S. Chatterjee, S. W. Koch, B. Kunert, and W. Stolz, "High-power optically pumped semiconductor laser at 1040 nm," *Photonics Technology Letters, IEEE*, vol. 22, no. 9, pp. 661–663, May 2010.

[6] J. M. Hopkins, S. A. Smith, C. W. Jeon, H. D. Sun, D. Burns, S. Calvez, M. D. Dawson, T. Jouhti, and M. Pessa, "0.6 W CW GaInNAs vertical external-cavity surface emitting laser operating at 1.32 μm," *Electronics Letters*, vol. 40, no. 1, pp. 30–31, Jan 2004.

[7] R. P. Sarzała and W. Nakwaski, "Optimization of 1.3 μm GaAs-based oxide-confined (GaIn)(NAs) vertical-cavity surface-emitting lasers for low-threshold room-temperature operation," *Journal of Physics: Condensed Matter*, vol. 16, no. 31, p. S3121, 2004.

[8] S. L. Chuang, *Physics of Optoelectronic Devices*. New York: John Wiley & Sons, 1995.

[9] L. Piskorski, L. Frasunkiewicz, A. K. Sokol, and R. P. Sarzala, "A possibility to achieve emission in the mid-infrared wavelength range from semiconductor laser active regions," in *Transparent Optical Networks (ICTON), 2014 16th International Conference on*, July 2014, pp. 1–4.

[10] A. K. Sokół and R. P. Sarzała, "Numerical analysis of optically pumped VECSELs," *Proceedings of SPIE*, vol. 8702, 2013.

[11] T. Leinonen, Y. A. Morozov, A. Harkonen, and M. Pessa, "Vertical external-cavity surface-emitting laser for dual-wavelength generation," *Photonics Technology Letters, IEEE*, vol. 17, no. 12, pp. 2508–2510, 2005.

[12] M. Wasiak, "Mathematical rigorous approach to simulate an over-threshold VCSEL operation," *Physica E: Low-dimensional Systems and Nanostructures*, vol. 43, no. 8, pp. 1439–1444, 2011.

[13] R. P. Sarzala, L. Piskorski, R. Szczerbiak, R. Kudrawiec, and W. Nakwaski, "An attempt to design long-wavelength (¿2 μm) InP-based GaInNAs diode lasers," *Applied Physics A*, vol. 108, no. 3, pp. 521–528, 2012.

[14] R. Fehse, S. Tomic, A. R. Adams, S. J. Sweeney, E. P. O'Reilly, A. Andreev, and H. Riechert, "A quantitative study of radiative, auger, and defect related recombination processes in 1.3-μm GaInNAs-based quantum-well lasers," *Selected Topics in Quantum Electronics, IEEE Journal of*, vol. 8, no. 4, pp. 801–810, Jul 2002.

[15] R. P. Sarzała and W. Nakwaski, "Carrier diffusion inside active regions of gain-guided vertical-cavity surface-emitting lasers," *Optoelectronics, IEE Proceedings -*, vol. 144, no. 6, pp. 421–425, Dec 1997.

[16] A. Amith, I. Kudman, and E. F. Steigmeier, "Electron and phonon scattering in GaAs at high temperatures," *Phys. Rev.*, vol. 138, pp. A1270–A1276, May 1965.

[17] S. Adachi, "GaAs, AlAs, and AlxGa1–xAs material parameters for use in research and device applications," *Journal of Applied Physics*, vol. 58, no. 3, pp. R1–R29, 1985.

[18] W. Nakwaski, "Thermal conductivity of binary, ternary, and quaternary III-V compounds," *Journal of Applied Physics*, vol. 64, no. 1, pp. 159–166, 1988.

[19] A. K. Sokół and R. P. Sarzała, "Comparative analysis of thermal problems in GaAs- and InP-based 1.3-μmVECSELs," *Optica Applicata*, vol. 43, no. 2, pp. 325–341, 2013.

[20] Y. S. Touloukian, R. W. Powell, C. Y. Ho, and P. G. Klemens, *Thermophysical Properties of Matter Volume 1: Thermal Conductivity: Metallic Elements and Alloys*. New York: IFI/Plenum, 1970.

[21] D. R. Lide, *CRC Handbook of Chemistry and Physics*. Boca Raton: CRC Press, 2005.

[22] S. Kasap and P. Capper, Eds., *Springer Handbook of Electronic and Photonic Materials*. Leipzig: Springer, 2007.

[23] S. Barman and G. P. Srivastava, "Temperature dependence of the thermal conductivity of different forms of diamond," *Journal of Applied Physics*, vol. 101, no. 12, pp. 123 507–8, 2007.

[24] S. Gehrsitz, F. K. Reinhart, C. Gourgon, N. Herres, A. Vonlanthen, and H. Sigg, "The refractive index of AlxGa1-xAs below the band gap: Accurate determination and empirical modeling," *Journal of Applied Physics*, vol. 87, no. 11, pp. 7825–7837, 2000.

[25] S. R. Adachi, *Physical Properties of III-V Semiconductor Compounds, 1st edition*. Chichester: John Wiley & Sons, 1992.

[26] W. K. Tan, H.-Y. Wong, A. E. Kelly, M. Sorel, J. H. Marsh, and A. C. Bryce, "Temperature behaviour of pulse repetition frequency in passively mode-locked InGaAsP/InP laser diode — experimental results and simple model," *Selected Topics in Quantum Electronics, IEEE Journal of*, vol. 13, no. 5, pp. 1209–1214, Sept 2007.

[27] T. Kitatani, M. Kondow, K. Shinoda, Y. Yazawa, M. Okai, and K. Uomi, "Extremely large refractive index of strained gainnas thin films," in *Indium Phosphide and Related Materials, 1998 International Conference on*, May 1998, pp. 341–344.